Perfect optical absorption with nanostructured metal films: design and experimental demonstration

GEORGE PERRAKIS,[1,2] ODYSSEAS TSILIPAKOS,[1,*] GEORGE KENANAKIS,[1,5] MARIA KAFESAKI,[1,2] COSTAS M. SOUKOULIS,[1,3] AND ELEFTHERIOS N. ECONOMOU[1,4]

[1]*Institute of Electronic Structure and Laser, FORTH GR-71110, Heraklion, Crete, Greece*
[2]*Department of Materials Science and Technology, University of Crete GR-71003, Heraklion, Crete, Greece*
[3]*Ames Laboratory—U.S. DOE and Department of Physics and Astronomy, Iowa State University, Ames, Iowa 50011, USA*
[4]*Department of Physics, University of Crete GR-71003, Heraklion, Crete, Greece*
[5]*gkenanak@iesl.forth.gr*
[*]*otsilipakos@iesl.forth.gr*

Abstract: Structuring metal surfaces on the nanoscale has been shown to alter their fundamental processes like reflection or absorption by supporting surface plasmon resonances. Here, we propose metal films with subwavelength rectangular nanostructuring that perfectly absorb the incident radiation in the optical regime. The structures are fabricated with low-cost nanoimprint lithography and thus constitute an appealing alternative to elaborate absorber designs with complex meta-atoms or multilayer structuring. We conduct a thorough numerical analysis to gain physical insight on how the key structural parameters affect the optical response and identify the designs leading to broad spectral and angular bandwidths, both of which are highly desirable in practical absorber applications. Subsequently, we fabricate and measure the structures with an FT-IR spectrometer demonstrating very good agreement with theory. Finally, we assess the performance of the proposed structures as sensing devices by quantifying the dependence of the absorption peak frequency position on the superstrate material.

1. Introduction

Surface plasmon polaritons (SPPs) are electromagnetic surfaces waves coupled to free electron oscillations [1–4]. They propagate along a metal-dielectric interface and exhibit an exponential decay of the field components away from it [1,2,4]. Free space radiation cannot couple directly to propagating SPPs due to the wavevector mismatch between them, i.e., the dispersion relation of SPP waves lies on the right of the light line. Thus, the excitation of SPPs exploiting corrugated metal-dielectric surfaces which can satisfy momentum conservation has been a subject of continuous research.

Following the seminal work of Raether [1], metallic corrugated surfaces and gratings have been investigated for an abundance of applications. Besides efficient coupling to propagating SPPs [5–7], metallic gratings can be used as Bragg reflectors to route propagating signals in guided wave circuits [8–11] or form wavelength-selective components [12–14]. In addition, they can serve as diffractive optical elements deflecting free-space beams to the desired direction [15,16]. Finally, they have been examined for demonstrating SPP-based sensors exploiting the field enhancement on the metallic-dielectric interface [17,18].

In this work, we focus on a different application, that of perfect absorption. Recently-proposed metamaterial-based perfect absorbers require elaborate designs with precisely structured metal inclusions and/or multilayer topologies [19–25]. Achieving efficient

operation with simpler structures that do not involve elaborate fabrication techniques is thus of high importance, as highlighted in [26]. Here, we design metal films with rectangular nanostructuring (i.e., binary metallic gratings with subwavelength pitch) that can perfectly absorb incident radiation without any reflections. The structures are designed to operate in the visible region. We propose broadband and wide-angle designs that are suitable for practical perfect absorption applications. We subsequently fabricate selected samples using nanoimprint lithography: a low-cost process that is particularly advantageous for producing large scale samples, something not possible with other fabrication techniques. We measure their optical response using Fourier-transform infrared spectroscopy and find excellent agreement between measured and simulated data. We are thus able to demonstrate experimentally an optical perfect absorber that offers excellent performance in terms of absorption efficiency and angular bandwidth and at the same time is a very simple structure that can be fabricated with a low cost fabrication technique. In addition, we find that the spectral position of the absorption peak is sensitive to the superstrate material. As a result, we highlight the possibility of utilizing our structures for sensing applications, thus allowing for multiple functionalities with the same structure by properly selecting the geometrical parameters in the design stage.

Other routes to simple and efficient absorber designs have been proposed in the literature. One prominent example is high-impedance structures, such as the mushroom structure [27,28]. Their main characteristic is wide-angle absorption, achieved by suppressing the spatial dispersion (angular dependence) of the surface input impedance. Fabricating mushroom structures for the microwave frequency regime is straightforward by means of plated through vias on standard printed circuit boards. However, this is not the case in the optical regime we are targeting. Another prominent example is planar, uniform multi-layer structures comprising lossy dielectric and metal layers [29,30]. In these cases, it becomes necessary to process different materials for covering different frequencies of operation [30]. Having a structure made of a single material that can tune its operation frequency by means of the geometrical parameters of the patterning is thus beneficial from a fabrication standpoint.

The remainder of the paper is organized as follows: The structure under study is presented in Section 2 along with the relevant geometrical and material parameters. In Section 3 we conduct a thorough numerical analysis to gain insight on how the key structural parameters affect the optical response and identify practical designs with broad spectral and angular bandwidth. Section 4 discusses the fabrication details and presents the experimental measurements verifying the numerical simulations. Finally, in Section 5 we quantify the dependence of the absorption peak position on the superstrate material.

2. Geometric and material parameters

The structure under study is the binary (i.e., rectangular) grating depicted in Fig. 1. It consists of metallic ridges of width s and height h on top of a metallic substrate with thickness t. In the remainder of the paper we assume $t = 200 \, \text{nm}$ meaning that for the wavelengths of interest (400-1200 nm) the structure is opaque and no transmission is allowed. The periodicity (pitch) is denoted by a. It is set to 400 nm (or lower) meaning that in the said wavelength range only the zeroth diffraction order is propagating (normal incidence). For the material parameters, the metal is silver and the relative permittivity, ε_m, is given by a Drude model, $\varepsilon_m = 1 - \omega_p^2 / (\omega^2 + i\omega\gamma)$, with plasma frequency $\omega_p = 13.2 \cdot 10^{15}$ rad/s and collision rate $\gamma = 43.33 \cdot 10^{13}$ rad/s [31]. Note that for the operating wavelengths considered in this work (longer than 400 nm) the permittivity of silver can be accurately described by a Drude dispersion model; interband transitions have a noticeable impact for shorter wavelengths. The relative permittivity of the superstrate material is ε_s and is initially set to 1 (air).

In what follows, we assess the optical response by illuminating the structure with a plane wave of TM polarization, $\mathbf{H} = H_z \hat{\mathbf{z}}$, impinging at an incidence angle θ (Fig. 1). We calculate or measure the reflection coefficient and subsequently determine the absorption through $A = 1 - R$ since transmission through the structure is zero.
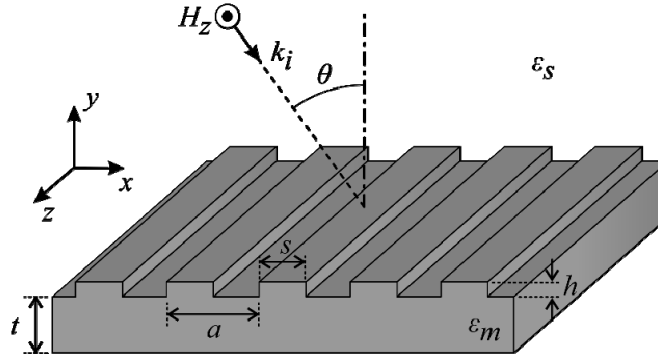

Fig. 1. Binary metallic grating illuminated by a TM polarized plane wave impinging at an incidence angle θ. All relevant geometric parameters (pitch a, ridge width s, and ridge height h) are included. $t = 200$ nm throughout the paper.

3. Optical response: perfect absorption in the visible regime

For calculating the optical response we conduct full-wave electromagnetic simulations using commercially available software (CST Microwave Studio, Computer Simulation Technology GmbH, Darmstadt, Germany). We start from normal incidence ($\theta = 0$) and vary the ridge height, h, while keeping the width, s, constant at 250 nm. The results are depicted in Fig. 2(a). The presence of a surface corrugation results in the excitation of SPPs on the metal-dielectric interface. This manifests as a reflection dip which translates into an absorption peak. For $h = 10$ nm, the grating can be considered a slight perturbation of the planar interface. This can be verified by the electric field distribution (real part of E_y component) which is included in Fig. 2(a) as an inset. As a result, the wavelength of the absorption peak is at 432 nm, very close to 424 nm calculated from the Bragg condition, $k_{\mathrm{SPP}} = k_0 \sqrt{\varepsilon_s} \sin\theta + m(2\pi / a)$, and the well-known dispersion relation for SPPs on metal-dielectric interfaces [1], which for normal incidence ($\theta = 0$) lead to:

$$k_{\mathrm{SPP}} = \frac{2\pi}{a} \Rightarrow k_0 \sqrt{\frac{\varepsilon_s \varepsilon_m(\omega)}{\varepsilon_s + \varepsilon_m(\omega)}} = \frac{2\pi}{a}, \tag{1}$$

where $k_0 = \omega / c_0$ is the wavenumber in vacuum and $\varepsilon_s = 1$ for an air superstrate.

By increasing the ridge height the position of the absorption peak redshifts [Fig. 2(a)]. In addition, the maximum absorption increases reaching 100% for $h = 20$ nm, indicating that the radiation reflected directly from the surface (the zeroth diffraction order) and the radiation out-coupled (scattered back to the radiation zone) from the propagating SPPs are equal and exactly out of phase. For $h \geq 30$ nm the absorption peak starts decreasing again since we deviate from the condition of perfect destructive interference leading to nonzero reflection. In addition, tuning the ridge height results in a strong variation of the absorption linewidth.

The increased absorption bandwidth observed for $h = 50$ nm in Fig. 2(a) is beneficial for perfect absorption applications. We thus retain this height value and vary the ridge width (i.e., the second design parameter) aiming to increase the absorption efficiency. The results are depicted in Fig. 2(b). Indeed, as the ridge width increases we observe an increase in the

absorption efficiency. To reveal the origin of this increase we plot the *E*-field norm distribution for three characteristic values of *s*: 250, 350, and 375 nm. As can be seen in Fig. 2(c), as *s* increases the field becomes tightly confined in the slot region between adjacent ridges. The field enhancement compared to the incident amplitude increases accordingly: 30, 40, and 45 in the three cases, respectively. The excitation of localized slot modes in metallic gratings has also been reported in [17,32]. The increased field enhancement associated with squeezing the field into a smaller slot volume leads to stronger absorption $(A \sim |\mathbf{E}|^2)$. We note that for $s > 375$ nm the absorption peak starts decreasing again (not shown) as the fields cannot be accommodated inside the nanoscale gaps.

In Fig. 2(d) we plot the maximum value of the absorption spectrum for any parameter combination in the entire (s, h) parametric space and in Fig. 2(e) the corresponding wavelength where it is observed. These plots can serve as a design guide for achieving perfect optical absorption with 100% efficiency at different wavelengths by properly tuning the geometrical parameters of the structure under study.
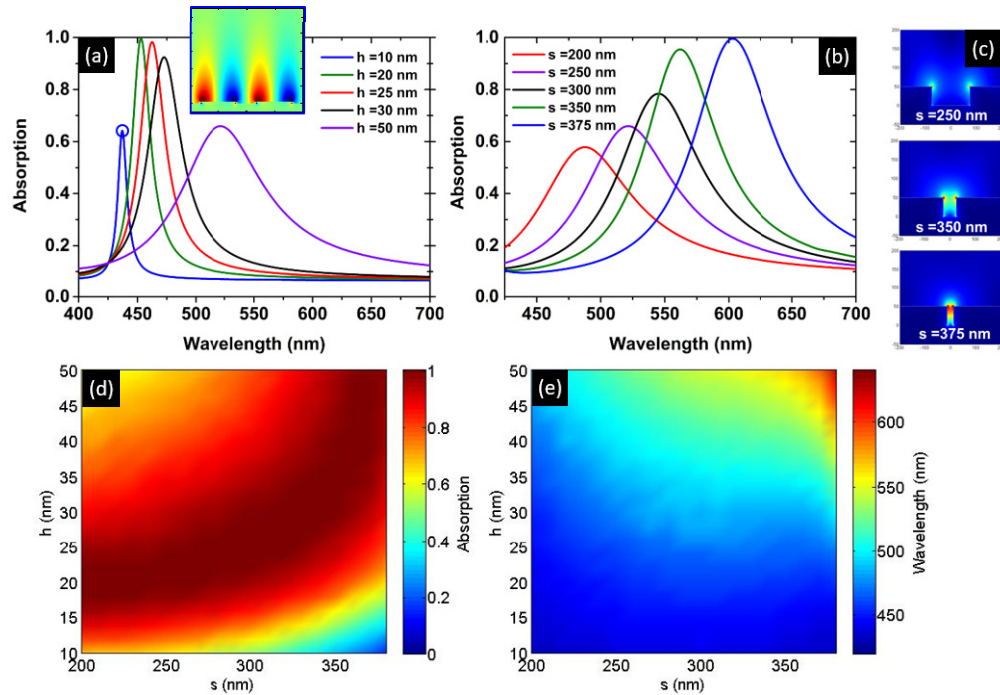

Fig. 2. (a) Absorption vs wavelength when varying the ridge height, *h*, while keeping the width constant at *s* = 250 nm. (b) Absorption vs wavelength when varying the ridge width, *s*, while keeping the height constant at *h* = 50 nm. (c) Electric field amplitude at the absorption peak (red denotes high values and blue low values). With increasing *s* the field becomes tightly confined in the slot and the field enhancement increases. (d) Maximum value of the absorption spectrum for any parameter combination in the entire (*s, h*) parametric space and (e) the corresponding wavelength where it is observed.

We are now interested in the performance of the proposed structure under oblique incidence, since this is important for practical perfect absorption applications. We first focus on the structure with $a = 400$ nm, $h = 50$ nm, and $s = 375$ nm that featured 100% absorption efficiency in Fig. 2(b). The incidence angle is varied up to 65° and the results are compiled in Fig. 3(a). The absorption remains quite high; however, the position of the peak moves to higher wavelengths and the absorption linewidth decreases. Note that as the incidence angle increases the onset of the first diffraction order approaches the wavelength of the main absorption peak and extra features are introduced in the absorption spectrum (lower

wavelengths). Markers in Fig. 3(a) denote the analytically calculated onset of the first diffraction order, taking place when the respective reflected wavevector (normal component) becomes real. This is further corroborated in Fig. 3(c), where we plot the field distribution (real part of scattered field, E_y component) for $\theta = 20°$ and $\lambda = 536$ nm [geometric parameters as in Fig. 3(a)]. It can be readily seen that the first diffraction order has just become propagating and is leaving the structure at grazing angle. It should be noted that when higher diffraction orders become propagating the relation between reflection and absorption coefficients is modified to $A = 1 - \sum_m R_m$, where index m runs through the propagating diffraction orders. In analogy with the sharp features in the absorption spectrum when a higher reflection diffraction order becomes propagating observed here (Fig. 3), sharp features in the transmissivity from a grating of cylindrical particles have been associated with the emergence of a higher refraction diffraction order in [33].

In Fig. 3(b) we alter the design: we retain the s/a ratio constant at the optimum value (375/400 = 0.9375) found in Fig. 2(b), but modify the grating pitch, a, to 275 nm. This way, higher diffraction orders do not approach the vicinity of the perfect absorption peak near ~600 nm even for very steep angles of incidence. As a result, the absorption peak shows exceptional robustness with incidence angle: the efficiency, position and linewidth of absorption remain unchanged for incidence angles up to 65°.
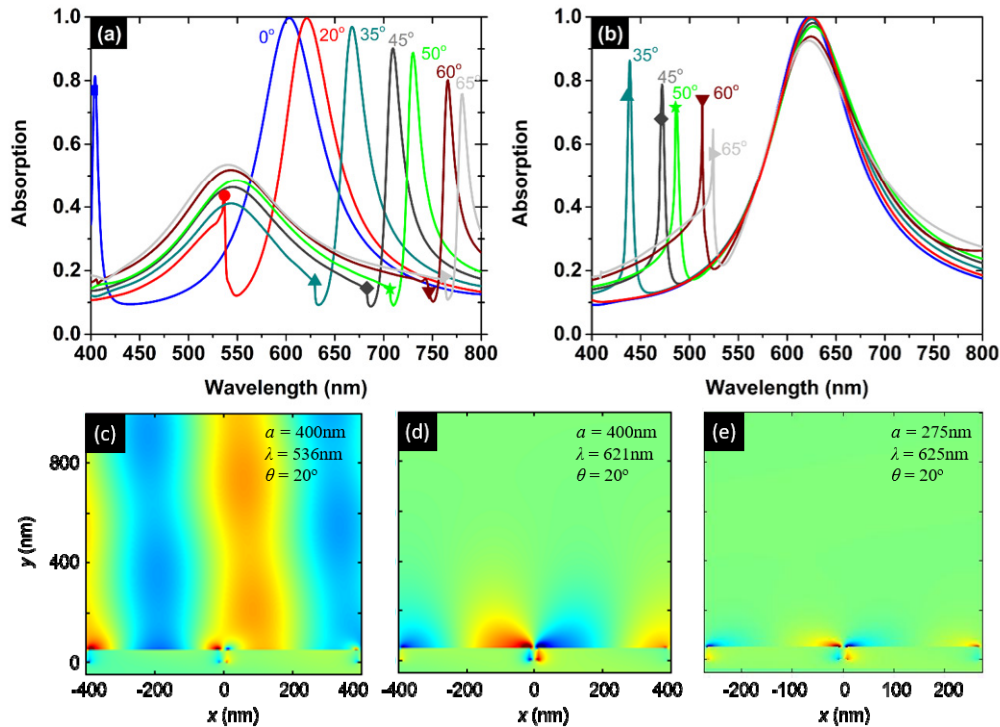

Fig. 3. (a) Absorption vs wavelength for varying incidence angle (TM polarization) when $a =$ 400 nm, $h = 50$ nm and $s = 0.9375a = 375$ nm. The absorption remains high but the position and linewidth of the peak change. (b) Absorption vs wavelength for varying incidence angle when $a = 275$ nm, $h = 50$ nm and $s = 0.9375a = 258$ nm. The efficiency, position and linewidth of absorption remain unchanged for incidence angles up to 65°. Markers denote the analytically calculated onset of the first diffraction order. Field distributions (real part of scattered E_y component) for three characteristic points: (c) At 536 nm on the 20-degree curve in panel (a). The first diffraction order has just become propagating and is leaving the structure at grazing angle. (d) At 621 nm on the 20-degree curve in panel (a).(e) At 625 nm on the 20-degree curve in panel (b).

The results in Figs. 2 and 3 highlight the existence and hybridization of two types of resonances in metallic gratings, which have been identified in the literature [32]. More specifically, one type of resonance is primarily an SPP with the E-field located mainly on the top surface of the ridges [see inset in Fig. 2(a) for example]. The second type concerns localized resonances inside the metal slots. When these resonances are tightly confined and do not hybridize with the SPP-type resonances, they are characterized by flat (dispersionless) bands in the (k_x, ω) photonic band diagram of the periodic structure [32]. In other words, the position of the corresponding spectral absorption feature does not depend on the incidence angle, which is the case seen in Fig. 3(b). This case of tightly confined fields inside the metal slots is depicted in Fig. 3(e) and corresponds to $\theta = 20^o$, $\lambda = 625$ nm, geometric parameters as in Fig. 3(b). Intermediate scenarios where the localized modes hybridize with the SPP-type resonance leading to dependence of the absorption peak with the incidence angle are seen in Fig. 3(a) for example. A characteristic corresponding field distribution is depicted in Fig. 3(d) and concerns the case $\theta = 20^o$ and $\lambda = 621$ nm [geometric parameters as in Fig. 3(a)].

To recapitulate, we have investigated how the key structural parameters (a, h, s) affect the optical response of our nanostructured metal film. Observing the results in Figs. 2, 3 one sees several opportunities for perfect absorption with the simple structure of a binary metallic grating. However, one should be careful in selecting the optimum design taking into account the absorption bandwidth and the robustness with incidence angle. The design in Fig. 3(b) satisfies both of these requirements by adopting a narrow slot region for confining the fields with increased enhancement and by opting for a short pitch value to avoid higher diffraction orders becoming propagating in the spectral vicinity of the absorption peak.

4. Experimental verification of perfect optical absorption

Next, we fabricate and measure two different samples in order to verify our proposed approach. Our structures were realized by means of ultraviolet nanoimprint lithography (UV-NIL). First, typical silicon (Si) master molds were realized by electron beam lithography and reactive ion etching steps. Each Si master mold was treated with an anti-adhesion coating to enhance the release properties of the mold during replication steps. Subsequently a soft PDMS (Sylgard 184, Dow Corning, USA) replica was fabricated by casting the PDMS pre-polymer against the relief structure of Si master molds. A 10:1 ratio (precursor: curing agent) was mixed and cured for 12 hours at 60 °C. The final PDMS mold was used as our working mold in the UV-NIL process. A thin layer of Ormocomp resist material (micro resist technology GmbH, Germany) was spin coated (3000 rpm for 1 min) on a silicon substrate while the PDMS mold and substrate were brought into physical contact. Once the cavities of the PDMS molds were filled, the assembly was exposed to soft air pressure (5bars) followed by a UV light (365 nm) exposure for 5 sec. Subsequently, our replicated structures were coated with a thin (200 nm) Ag layer by means of evaporation.

For the experimental electromagnetic characterization we performed FT-IR measurements using a Bruker Vertex 70v spectrometer with a collimated beam, attached to a Bruker HYPERION 2000 FT-IR microscope, and two calcite based Glan-Thompson linear polarizers, providing a >500:1 degree of polarization in a spectral range of 450 nm. The above instrument was equipped with a Quartz beamsplitter and a room temperature RT-Silicon diode detector, in order to get both transmission and reflection measurements in a spectral range of 400-900 nm (25.000 – 11.100 cm^{-1}). A total of 100 scans were acquired with a scanner velocity of 10 kHz at a resolution of 8 cm^{-1}. The scans were coadded, apodized with the Blackman-Harris three-term function, and fast Fourier transformed with two level of zero filling to produce spectral data encoded at 0.2 cm^{-1} intervals.

The measured data are presented in Fig. 4 (solid curves) for two different designs and compared with the respective simulations (dashed curves). More specifically, Fig. 4(a) concerns the design $(a, h, s) = (400$ nm, 50 nm, 375 nm) and Fig. 4(b) the design $(a, h, s) = (400$ nm, 20 nm, 200 nm). In both cases, very good agreement between theory and

experiment is observed, indicating the high quality of the fabricated samples and validating the numerical simulations. Deviations in the absorption peak position are minimal and a slight discrepancy in the absorption linewidth can be attributed to sample roughness. The ripple in Fig. 4(b) is due to measuring near the limit of the FT-IR spectrometer's range. The surface morphology of the samples was studied by means of a field emission scanning electron microscope (FE-SEM, JEOL JSM-7000F). The SEM image appearing as an inset in Fig. 4(b) demonstrates that the actual dimensions of the fabricated sample are in excellent agreement with the nominal values.
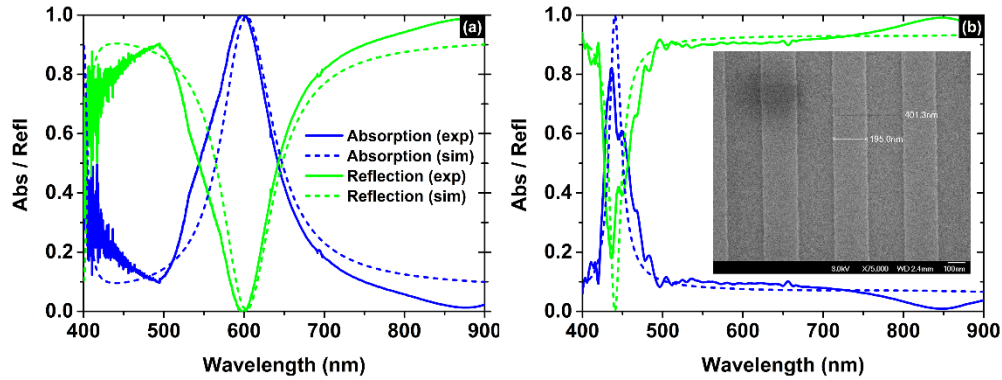

Fig. 4. Simulated and measured reflection and absorption spectra for (a) the design (a, h, s) = (400 nm, 50 nm, 375 nm) and (b) the design (a, h, s) = (400 nm, 20 nm, 200 nm). Excellent agreement between simulation and experiment is observed. The SEM image inset in panel (b) demonstrates that the actual dimensions of the fabricated sample are in excellent agreement with the nominal values.

5. Effect of superstrate material

In this section, we investigate the effect of the superstrate permittivity on the optical response of our proposed structure. We are interested in assessing the potential of the structure as a sensing platform. In Fig. 5 we examine different analytes (amines, acids, etc.) relevant for sensing applications. We focus on the design with $a = 400$ nm, $h = 20$ nm, and $s = 200$ nm examined in Fig. 4(b) since a smaller linewidth is preferable for sensing applications. As the superstrate permittivity changes (increases) the absorption peak experiences a significant shift towards higher wavelengths. More specifically, the absorption peaks shifts from $\lambda_{PA} = 440$ nm for air, to $\lambda_{PA} = 700$ nm for $C_4H_{11}N$ ($\varepsilon_r = 3.6$), $\lambda_{PA} = 793$ nm for $CHCl_3$ ($\varepsilon_r = 4.8$), and $\lambda_{PA} = 900$ nm for HCl ($\varepsilon_r = 6.35$). Importantly, the absorption efficiency is retained at 100%. As a result, tracking the position of the perfect absorption peak, appearing as a reflection dip in actual measurements, allows for identifying the permittivity of the material covering our binary metallic grating structure.
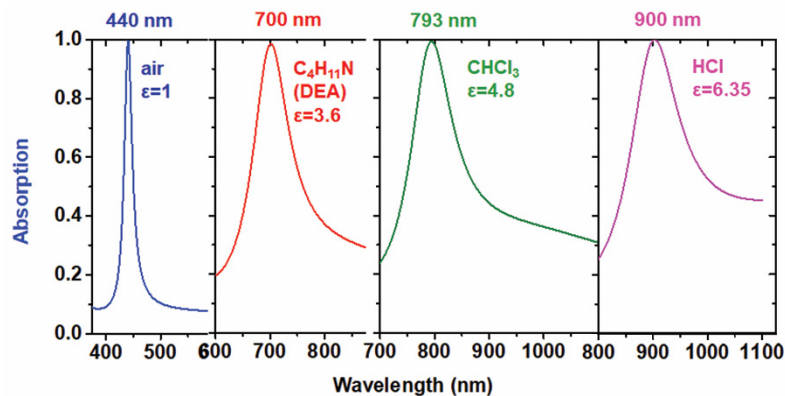
Fig. 5. Response of metallic binary grating with $(a, h, s) = (400\,\text{nm}, 20\,\text{nm}, 200\,\text{nm})$ for different superstrate materials. The absorption peak is significantly shifted towards higher wavelengths while maintaining 100% absorption efficiency.

6. Conclusions

We have demonstrated, both theoretically and experimentally, perfect optical absorption using simple metallic films with a subwavelength rectangular nanostructuring. Such corrugated films can be easily fabricated with low-cost nanoimprint lithography and thus constitute an appealing alternative to elaborate absorber structures. We have conducted a thorough numerical analysis to identify the design that results in both broad absorption bandwidth and angle-independent performance, both of which are essential traits for an efficient absorber structure. To verify the theoretical results, two samples were fabricated and subsequently measured with an FT-IR spectrometer; very good agreement with the numerical simulations has been observed. Finally, we have assessed the potential of the proposed structures as refractive index sensing devices by examining the effect of the superstrate material on the absorption spectrum.

Funding

References

1. H. Raether, *Surface Plasmons on Smooth and Rough Surfaces and on Gratings* (Springer-Verlag, 1988).
2. E. N. Economou, "Surface plasmons in thin films," Phys. Rev. **182**(2), 539–554 (1969).
3. W. L. Barnes, A. Dereux, and T. W. Ebbesen, "Surface plasmon subwavelength optics," Nature **424**(6950), 824–830 (2003).
4. O. Tsilipakos, T. V. Yioultsis, and E. E. Kriezis, "Theoretical analysis of thermally tunable microring resonator filters made of dielectric-loaded plasmonic waveguides," J. Appl. Phys. **106**(9), 093109 (2009).
5. A. V. Krasavin and N. I. Zheludev, "Active plasmonics: Controlling signals in Au/Ga waveguide using nanoscale structural transformations," Appl. Phys. Lett. **84**(8), 1416–1418 (2004).
6. I. P. Radko, S. I. Bozhevolnyi, G. Brucoli, L. Martín-Moreno, F. J. García-Vidal, and A. Boltasseva, "Efficiency of local surface plasmon polariton excitation on ridges," Phys. Rev. B Condens. Matter Mater. Phys. **78**(11), 115115 (2008).
7. V. M. Shalaev and S. Kawata, eds., *Nanophotonics with Surface Plasmons* (Elsevier, 2007).
8. M. U. González, J.-C. Weeber, A.-L. Baudrion, A. Dereux, A. L. Stepanov, J. R. Krenn, E. Devaux, and T. W. Ebbesen, "Design, near-field characterization, and modeling of 45 surface-plasmon Bragg mirrors," Phys. Rev. B Condens. Matter Mater. Phys. **73**(15), 155416 (2006).
9. S. Jetté-Charbonneau, R. Charbonneau, N. Lahoud, G. Mattiussi, and P. Berini, "Demonstration of Bragg gratings based on long-ranging surface plasmon polariton waveguides," Opt. Express **13**(12), 4674–4682 (2005).
10. S. Jetté-Charbonneau, R. Charbonneau, N. Lahoud, G. A. Mattiussi, and P. Berini, "Bragg gratings based on long-range surface plasmon-polariton waveguides: comparison of theory and experiment," IEEE J. Quantum

Electron. **41**(12), 1480–1491 (2005).

11. S. I. Bozhevolnyi, A. Boltasseva, T. Søndergaard, T. Nikolajsen, and K. Leosson, "Photonic bandgap structures for long-range surface plasmon polaritons," Opt. Commun. **250**(4-6), 328–333 (2005).

12. A. Boltasseva, S. Bozhevolnyi, T. Søndergaard, T. Nikolajsen, and K. Leosson, "Compact Z-add-drop wavelength filters for long-range surface plasmon polaritons," Opt. Express **13**(11), 4237–4243 (2005).

13. D. C. Zografopoulos and R. Beccherelli, "Liquid-crystal-tunable metal–insulator–metal plasmonic waveguides and Bragg resonators," J. Opt. **15**(5), 055009 (2013).

14. T. Christopoulos, G. Sinatkas, O. Tsilipakos, and E. E. Kriezis, "Bistable action with hybrid plasmonic Bragg-grating resonators," Opt. Quantum Electron. **48**(2), 128 (2016).

15. I. Epstein, I. Dolev, D. Bar-Lev, and A. Arie, "Plasmon-enhanced Bragg diffraction," Phys. Rev. B Condens. Matter Mater. Phys. **86**(20), 205122 (2012).

16. I. Dolev, I. Epstein, and A. Arie, "Surface-plasmon holographic beam shaping," Phys. Rev. Lett. **109**(20), 203903 (2012).

17. X. Sun, X. Shu, and C. Chen, "Grating surface plasmon resonance sensor: angular sensitivity, metal oxidization effect of Al-based device in optimal structure," Appl. Opt. **54**(6), 1548–1554 (2015).

18. Y.-L. Ho, L.-C. Huang, E. Lebrasseur, Y. Mita, and J.-J. Delaunay, "Independent light-trapping cavity for ultra-sensitive plasmonic sensing," Appl. Phys. Lett. **105**(6), 061112 (2014).

19. N. I. Landy, S. Sajuyigbe, J. J. Mock, D. R. Smith, and W. J. Padilla, "Perfect metamaterial absorber," Phys. Rev. Lett. **100**(20), 207402 (2008).

20. K. Aydin, V. E. Ferry, R. M. Briggs, and H. A. Atwater, "Broadband polarization-independent resonant light absorption using ultrathin plasmonic super absorbers," Nat. Commun. **2**(1), 517 (2011).

21. G. Isić, B. Vasić, D. C. Zografopoulos, R. Beccherelli, and R. Gajić, "Electrically tunable critically coupled terahertz metamaterial absorber based on nematic liquid crystals," Phys. Rev. Appl. **3**(6), 064007 (2015).

22. D. C. Zografopoulos, G. Sinatkas, E. Lotfi, L. A. Shahada, M. A. Swillam, E. E. Kriezis, and R. Beccherelli, "Amplitude modulation in infrared metamaterial absorbers based on electro-optically tunable conducting oxides," Appl. Phys., A Mater. Sci. Process. **124**(2), 105 (2018).

23. J. Hao, J. Wang, X. Liu, W. J. Padilla, L. Zhou, and M. Qiu, "High performance optical absorber based on a plasmonic metamaterial," Appl. Phys. Lett. **96**(25), 251104 (2010).

24. K. Bhattarai, S. Silva, K. Song, A. Urbas, S. J. Lee, Z. Ku, and J. Zhou, "Metamaterial Perfect Absorber Analyzed by a Meta-cavity Model Consisting of Multilayer Metasurfaces," Sci. Rep. **7**(1), 10569 (2017).

25. K. Bhattarai, Z. Ku, S. Silva, J. Jeon, J. O. Kim, S. J. Lee, A. Urbas, and J. Zhou, "A Large-Area, Mushroom-Capped Plasmonic Perfect Absorber: Refractive Index Sensing and Fabry-Perot Cavity Mechanism," Adv. Opt. Mater. **3**(12), 1779–1786 (2015).

26. G. Kenanakis, C. P. Mavidis, E. Vasilaki, N. Katsarakis, M. Kafesaki, E. N. Economou, and C. M. Soukoulis, "Perfect absorbers based on metal-insulator-metal structures in the visible region: a simple approach for practical applications," Appl. Phys., A Mater. Sci. Process. **123**(1), 77 (2017).

27. S. A. Tretyakov and S. I. Maslovski, "Thin absorbing structure for all incidence angles based on the use of a high-impedance surface," Microw. Opt. Technol. Lett. **38**(3), 175–178 (2003).

28. H. Wakatsuchi, S. Kim, J. J. Rushton, and D. F. Sievenpiper, "Circuit-based nonlinear metasurface absorbers for high power surface currents," Appl. Phys. Lett. **102**(21), 214103 (2013).

29. M. A. Kats and F. Capasso, "Optical absorbers based on strong interference in ultra-thin films," Laser Photonics Rev. **10**(5), 735–749 (2016).

30. A. N. Papadimopoulos, N. V. Kantartzis, N. L. Tsitsas, and C. A. Valagiannopoulos, "Wide-angle absorption of visible light from simple bilayers," Appl. Opt. **56**(35), 9779–9786 (2017).

31. I. R. Hooper and J. R. Sambles, "Some considerations on the transmissivity of thin metal films," Opt. Express **16**(22), 17249–17257 (2008).

32. F. J. García-Vidal and L. Martín-Moreno, "Transmission and focusing of light in one-dimensional periodically nanostructured metals," Phys. Rev. B Condens. Matter Mater. Phys. **66**(15), 155412 (2002).

33. Z. Tagay and C. Valagiannopoulos, "Highly selective transmission and absorption from metasurfaces of periodically corrugated cylindrical particles," Phys. Rev. B **98**(11), 115306 (2018).